Synchronous Pre-biasing of Triboelectric Nanogenerator for Enhanced Energy Extraction

Madhav Pathak, *Graduate Student Member, IEEE*, and Ratnesh Kumar, *Fellow, IEEE*

***Abstract*—Triboelectric nanogenerator (TENG) is a class of ambient mechanical energy harvesters used to augment the battery life of electronic devices such as sensors in implantables, wearables, and internet of things applications. In this work, the fundamentals of pre-biasing (precharging) the TENG at the start of the operation cycle to enhance the percycle extracted energy is presented. The energy gain is mathematically formulated, and the optimum pre-biasing voltage (equivalently charge) is derived by analyzing the energy exchange between the mechanical and the electrical domain over a periodic cycle. Further, a novel energy extraction circuit (EEC) termed as "pre-biased synchronous charge extraction (pSCE)" is introduced to 1) realize synchronous pre-biasing of TENG using the load battery itself and 2) achieve enhanced energy extraction from TENG. Energy output percycle is derived analytically for the pSCE circuit and compared to the state of the art synchronous charge extraction (SCE) circuit. The experimental implementation is performed for the proposed pSCE circuit that shows a 6.65 fold gain over the full wave rectifier (standard EEC) and 1.45 over the SCE circuit for a 5 V battery load.**

***Index Terms*—Energy harvesting, pre-biasing, switched circuits, triboelectric nanogenerator (TENG).**

I. Introduction

WIRELESS sensor nodes used in the internet of things (IoT), wearable, and implantable applications are commonly powered by an onboard battery. Harnessing the ambient mechanical energy via an integrated energy harvester to charge the onboard battery is a green solution to prolonging the battery life [1]. Recently, developed triboelectric nanogenerator (TENGs) involving friction-induced triboelectrification and electrostatic induction have shown promising potential as versatile mechanical-to-electrical energy transducers [2], [3]. TENGs with its almost universal choice of materials and multiple operation modes [2] have been shown to harvest energy from variety of sources such as wind/water flow [4]–[6], machine/structure vibration [7], human body motion [8], [9], etc.

Motion transduction by TENG leads to variable output that needs rectification to charge dc battery load, and thus, full wave rectifier (FWR) can be considered the simplest energy extraction circuit (EEC) [10]. Approaches to enhance TENG's energy output require improving the source to load matching. To this end, several novel EEC architectures have been proposed in the literature to increase the energy output beyond the FWR circuit such as [11]–[17]. It is shown in [11] that all these different EEC outputs are confined within the cycle for maximized energy output (CMEO), where the *synchronously serial switched flyback converter with the rectified TENG output* can achieve the CMEO irrespective of the load value [14], [17]–[19]. This last architecture has been proposed previously in the piezoelectric context [20]–[22], by the name of synchronous charge extraction (SCE), which is how we also refer to it in this article.

The aforementioned EECs may be viewed as *passive EECs*, where no harvested energy is fed back to the TENG. In this work, we propose synchronous *pre-biasing* (or precharging) of TENG by feeding back some of the load battery energy to the TENG, thereby realizing an *"active" EEC*, which enables to achieve a net output beyond the CMEO limit. Here, synchronous pre-biasing refers to charging the TENG capacitor at the start of each half-cycle (at the minimum and maximum separation of TENG plates) by using the battery. During the separation phase, pre-biasing increases the electrostatic force between the two TENG plates and thereby the transduced energy in form of work done against it by the mechanical source, while during the contraction phase, pre-biasing reduces the TENG charge to zero for no loss of stored potential electrical energy to the environment. This work provides the following major contributions.

1) A novel EEC termed as "pre-biased pSCE" is introduced for the first time for synchronous energy extraction in-tandem with synchronous pre-biasing of TENG.
2) The percycle energy output of the proposed pSCE circuit is mathematically derived and is shown to exceed the SCE circuit's CMEO output at all load voltages.
3) Upper limits and optimum values, if any, on the pre-biasing voltage for each half-cycle of TENG operation are mathematically derived by analyzing the interplay of mechanical motion and electrostatic forces.
4) The experimental implementation of the pSCE circuit along with its synchronous switching controller is also

Manuscript received January 6, 2022; revised March 10, 2022; accepted April 19, 2022. Date of publication April 26, 2022; date of current version June 24, 2022. This work was supported in part by the U.S. National Science Foundation under Grant NSF-PFI-2141084 and Grant NSF-CSSI-2004766, and in part by the Iowa State University under Regents Innovation Fund. Recommended for publication by Associate Editor K.-H. Chen. *(Corresponding author: Madhav Pathak.)*

The authors are with the Department of Electrical and Computer Engineering, Iowa State University, Ames, IA 50011 USA (e-mail: mpathak@iastate.edu; rkumar@iastate.edu).

Supplementary notes for this work are available with the online version of the work are available at https://doi.org/10.1109/TPEL.2022.3169733. Our conference paper [DOI: 10.1109/SENSORS43011.2019.8956938] studied the pSCE circuit analyzed here in a rudimentary way and also without any experimental validation.

This article has supplementary material provided by the authors and color versions of one or more figures available at https://doi.org/10.1109/TPEL.2022.3169733.

Digital Object Identifier 10.1109/TPEL.2022.3169733

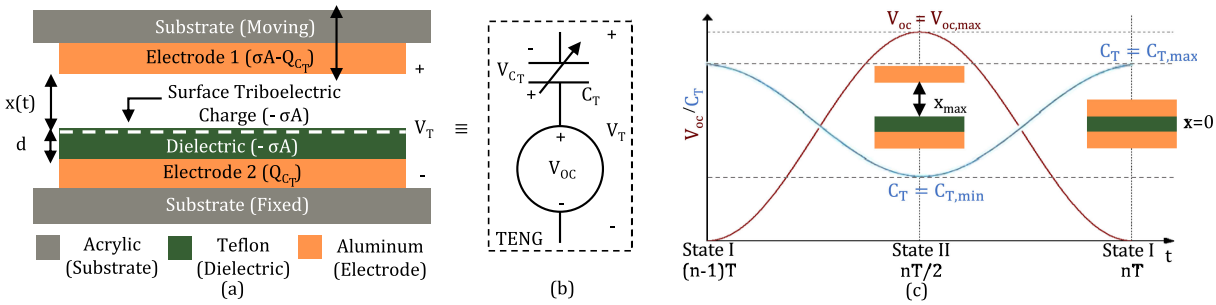

Fig. 1. (a) Cross section view of a contact-separation TENG. (b) Equivalent circuit model of TENG. (c) Periodic variation of open-circuit voltage ($V_{\rm oc}(t)$) and TENG capacitance ($C_T(t)$) over a period of time T.

presented, and an output gain of 1.45x over its peer SCE circuit and 6.65x over the standard FWR circuit is experimentally achieved. The comparative advantage over those reported in prior works [12]–[17], [23]–[28] is also reported, along with a *quantitative* comparison summarized in Table V.

Note that while we perform pre-biasing using the load battery itself, this can also be achieved by feeding back a fraction of the output charge [28]–[30] or also by the use of *LC* circuit oscillation, i.e., by using a parallel or series synchronous switched harvesting on inductor (P-SSHI/S-SSHI) circuit as EECs, as presented in our earlier works [23], [24] and in [25]–[27]. A key advantage of the proposed pSCE circuit as derived in this work is a guaranteed output beyond CMEO at all load voltages, unlike P-SSHI, S-SSHI EECs that may require additional power-consuming maximum power point tracking (MPPT) circuit to operate at their optimal load and to exceed the CMEO [24].

Also, it should be stated that while pSCE circuit architecture has been explored previously for piezoelectric transducers [21], [31], the analysis is entirely different in the case of triboelectric transducers since it has a different circuit model: For a piezoelectric transducer, capacitor appears in *parallel* to the source and is *fixed*, whereas the triboelectric capacitor appears in *series* and is *time-varying*. The work reported here innovates to deal with this time-varying nature by *smart discretization*, i.e., by performing analysis at the two extremities (plates fully contracted versus separate); *no such discretization is needed in the piezoelectric case* as the same set of time-invariant equations remain valid at all instances. The triboelectric analysis framework is thus much more intricate and has been developed in the presented generality for the first time. Also, owing to the above differences in the circuit model, the switching control circuits of the piezoelectric setting do not work in the TENG setting, and new switching circuits have been devised for the experimental implementation.

II. Preliminaries: TENG Model

The most generic form of TENG operation is in contact-separation mode where, as depicted in Fig. 1(a), the two parts of the TENG, namely, a metal film acting as electrode 1 (upper Al plate here) and a metal film covered with dielectric acting as electrode 2 (bottom Al plate covered with a Teflon tape) repeatedly comes in contact and separates under the influence of an external motion. Repeated contact-separation between the two plates generates equal and opposite triboelectric static charges on the two plates, with density, denoted σ. Ignoring the fringing field effect, the resulting field is given by

$$\vec{E_\sigma} = \frac{-\sigma}{\epsilon_0}\vec{1}_x \tag{1}$$

where ϵ_0 is the electrical permittivity of air, and $\vec{1}_x$ is the unit vector pointing upwards in the direction of increasing x. The voltage induced between the two electrodes by the above electric field is termed as open-circuit voltage and is given by

$$V_{\rm oc}(t) = -\int_0^{x(t)} \vec{E_\sigma}.\vec{1}_x dx = \frac{\sigma x(t)}{\epsilon_0}. \tag{2}$$

Also, TENG forms a variable capacitor with air gap, $x(t)$ and dielectric of thickness d between the two electrodes

$$C_T(t) = \frac{\epsilon_0 A}{x(t) + d_{\rm eff}}; \quad d_{\rm eff} = \frac{d}{\epsilon_d}.$$

Here, A is the contact surface area of the plates, and ϵ_d is the relative permittivity of the dielectric layer, lowering its effective thickness to $d_{\rm eff}$.

When TENG is connected to an external circuit, the movement of the conduction charge (distinct from the triboelectric charge) from one electrode to another, say $Q_{C_T}(t)$ [Refer Fig. 1(a)], leads to a capacitor voltage, $V_{C_T}(t)$ between the two electrodes. Thus, the net TENG voltage (V_T) is the superposition of open-circuit voltage ($V_{\rm oc}$), owing to the static triboelectric charge and its induced electrostatic emf, and the TENG capacitor voltage (V_{C_T}), owing to the free conduction charges on the electrodes

$$V_T(t) = V_{\rm oc}(t) - V_{C_T}(t) = \frac{\sigma x(t)}{\epsilon_0} - \frac{Q_{C_T}(t)}{C_T(t)}. \tag{3}$$

The above TENG operating equation leads to the circuit model shown in Fig. 1(b) with a variable voltage source ($V_{\rm oc}(t)$) in series with a variable capacitor ($C_T(t)$) [32].

As visualized in Fig. 1(c), we designate one extremity of TENG operation, where the two plates are in contact ($x(t) = 0$) as State I. While State II designates the other extremity of the TENG operation, where the two plates are maximally apart ($x(t) = x_{\rm max}$). TENG electrical parameters $V_{\rm oc}$ and C_T at these two states are listed in Table I. Further for analysis convenience, a system constant, ratio of maximum to minimum capacitance,

TABLE I
TENG PARAMETERS AT THE OPERATION EXTREMES

Operation State	Airgap (x)	Capacitance (C_T)	Open-circuit voltage (V_{oc})
State I	$x_{\min}=0$	$C_{T,\max}=\frac{\epsilon_0 A}{d_{eff}}$	$V_{\text{oc,min}}=0$
State II	$x_{\max}$	$C_{T,\min}=\frac{\epsilon_0 A}{x_{\max}+d_{\text{eff}}}$	$V_{\text{oc,max}}=\frac{\sigma x_{\max}}{\epsilon_0}$

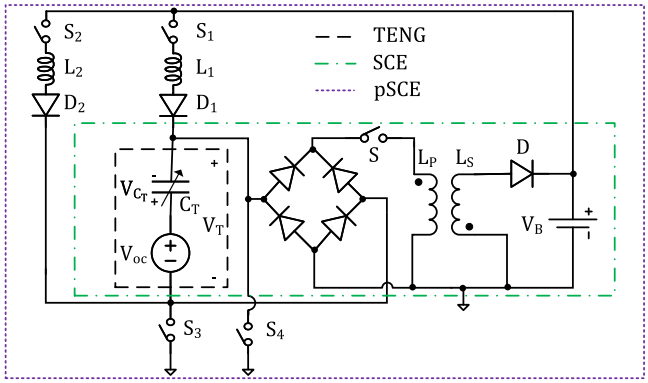

Fig. 2. SCE and pSCE circuit diagram (SCE portion of pSCE is enclosed in the green box).

is introduced

$$\beta=\frac{C_{T,\max}}{C_{T,\min}}=\frac{x_{\max}+d_{\text{eff}}}{d_{\text{eff}}}=\frac{x_{\max}}{d_{\text{eff}}}+1. \tag{4}$$

III. SYNCHRONOUS CHARGE EXTRACTION

The circuit in the green box of Fig. 2 represents the SCE circuit obtained by cascading a FWR with the flyback converter [14], [17], [18]. With switch S open, TENG achieves its high open-circuit maximum voltage ($V_{\text{oc,max}}$). An efficient energy transfer is made possible by closing the switch S at the extremes (States I and II), thereby forming a L_P-C_T oscillator and enabling the transfer of C_T energy to L_P (in one-quarter of the oscillation cycle), and subsequently transferring that energy to the load through L_s. Here, we start by deriving the TENG voltage and charge at the extremes (States I and II) and use those to derive the percycle energy extracted, confirming that it equals the CMEO. This then serves as a baseline for comparing the achieved gain in the extracted energy when pre-biasing is incorporated.

A. SCE Operation

The SCE circuit operation can be understood by following the operation cycle diagram of Fig. 3(a) and the TENG voltage waveform of Fig. 4(a). The cycle starts with the two plates pressed together ($x=0$) with TENG voltage (V_T) and TENG capacitor charge (Q_{C_T}) being zero. The switch S is opened, and as the two plates are separated, TENG voltage increases with TENG operating in open-circuit condition. When the plates are maximally apart, V_T reaches the maxima, with Q_{C_T} still being zero. This is State II [right top of Fig. 3(a)], with

$$V_T^{II}=V_{\text{oc,max}};\quad Q_{C_T}^{II}=0\Rightarrow V_{C_T}^{II}=0.$$

At this point, switch S is closed resulting in State II+ [right bottom of Fig. 3(a)] and simplifying the circuit to to a L_p-$C_{T,\min}$ oscillator as shown in the right half of Fig. 3(b). Then, the differential equation evolution of the TENG capacitor voltage satisfies

$$\frac{d^2V_{C_T}(t)}{dt^2}+\frac{V_{C_T}(t)}{L_PC_{T,\min}}-\frac{V_{\text{oc,max}}}{L_PC_{T,\min}}=0. \tag{5}$$

Above can be solved with initial condition as $V_{C_T}(0)=V_{C_T}^{II}=0$ to obtain

$$V_{C_T}(t)=-V_{\text{oc,max}}\cos\left(\omega_{\text{SCE}}^{II+}t\right)+V_{\text{oc,max}}$$
$$\omega_{\text{SCE}}^{II+}=\frac{1}{\sqrt{L_PC_{T,\min}}}$$

where $\omega_{\text{SCE}}^{II+}$ is the resonance frequency of the oscillator. Switch S is kept closed for one-fourth the L_P-$C_{T,\min}$ oscillation cycle, yielding

$$V_{C_T}^{II+}:=V_{C_T}\left(\frac{\pi}{2\omega_{\text{SCE}}^{II+}}\right)=V_{C_T}\left(T_{\text{SCE}}^{II+}\right)=V_{\text{oc,max}}$$

where T_{SCE}^{II+} denotes the switch-closure time at State II. At this point, the TENG capacitor voltage is the opposite of the TENG voltage source, and the overall TENG voltage V_T^{II+} has dropped to zero (from the TENG operating equation [see (3)]). Then, the TENG capacitor charge $Q_{C_T}^{II+}$ can be derived as

$$V_T^{II+}=V_{\text{oc,max}}-V_{C_T}^{II+}=V_{\text{oc,max}}-V_{\text{oc,max}}=0$$
$$Q_{C_T}^{II+}=C_T^{II+}V_{C_T}^{II+}=C_{T,\min}V_{\text{oc,max}}. \tag{6}$$

Thus, during T_{SCE}^{II+}, the TENG voltage ($V_T(t)$) falls from the maxima ($V_{\text{oc,max}}$) to zero, while the current in the loop ($I_{L_P}(t)$) rises sinusoidally from zero to it's maxima ($I_{L_P,\max}^{II+}$) [refer to "blue" curve of Fig. 3(c)]. During this time period the current in the secondary inductor L_S is blocked by the reverse-biased diode D, with the energy transferred from TENG being stored as magnetic energy in the core of transformer. On opening the switch S after T_{SCE}^{II+}, the primary inductor current quickly falls to zero while the secondary inductor current shoots up to $I_{L_P,\max}^{II+}$ (for turns ratio = 1), which in turn linearly decays to charge the load battery. Note that since the switching period T_{SCE}^{II+} is designed to be minuscule compared to the TENG operation period (T), the TENG capacitance $C_T(t)$ and open-circuit voltage $V_{\text{oc}}(t)$ are considered unchanged at $C_{T,\min}$ and $V_{\text{oc,max}}$, respectively, during the switching period.

With the start of second half-cycle, upper plate moves downward with switch S open, to reach the starting position ($x=0$) and State I is achieved [left bottom of Fig. 3(a)]. Due to open-circuit operation, the charge on the TENG capacitor is retained from State II+, however, the capacitance changes from $C_{T,\min}$ to $C_{T,\max}$, while the open-circuit voltage ($V_{\text{oc}}(t)$) falls to zero [Fig. 1(c)]. Thus

$$Q_{C_T}^{I}=Q_{C_T}^{II+}=C_{T,\min}V_{\text{oc,max}}$$
$$V_T^I=V_{\text{oc,min}}-V_{C_T}^I=0-\frac{Q_{C_T}^I}{C_{T,\max}}=-\frac{V_{\text{oc,max}}}{\beta}. \tag{7}$$

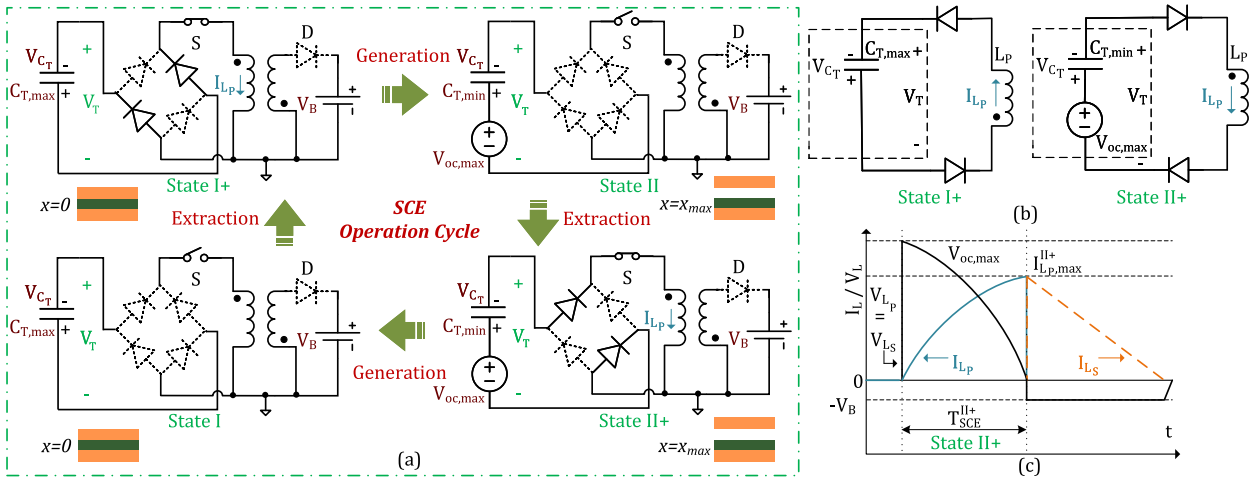

Fig. 3. SCE Circuit (a) operation cycle, (b) simplified circuit during energy extraction States I+ and II+ and (c) primary inductor current (I_{L_P}), voltage (V_{L_P}) and, secondary inductor current (I_{L_S}) during switching at State II.

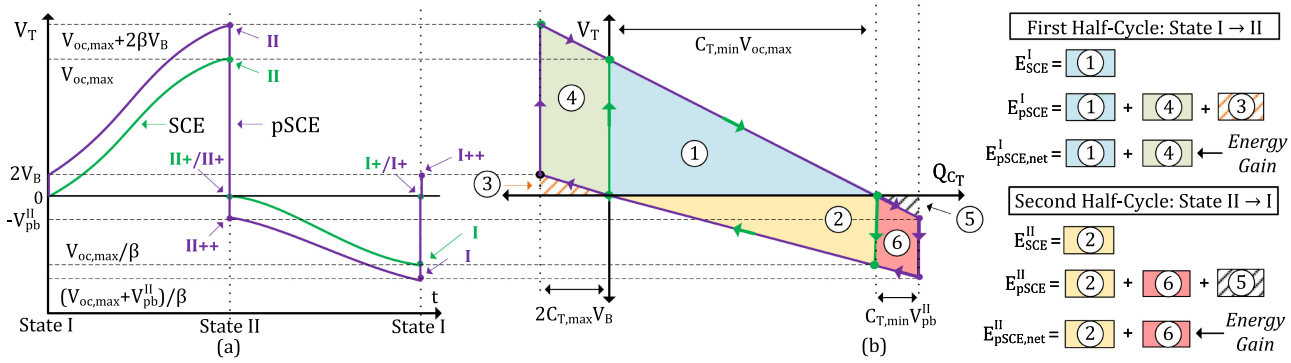

Fig. 4. (a) TENG voltage waveform plot (green under SCE vs. purple under pSCE). End of different circuit operation states are marked on both the waveforms. (b) TENG voltage versus charge ($V_T - Q_{C_T}$) plot for SCE (areas 1-2) and pSCE (areas 1-6).

To extract the TENG energy, switch S is closed for one-fourth the L_P-$C_{T,\max}$ oscillation cycle, entering State I+ [left top of Fig. 3(a)], with oscillation frequency and switch S closure time given by

$$\omega_{\text{SCE}}^{I+} = \frac{1}{\sqrt{L_P C_{T,\max}}}; T_{\text{SCE}}^{I+} = \frac{\pi}{2\omega_{\text{SCE}}^{I+}} = \sqrt{\beta} T_{\text{SCE}}^{II+}. \quad (8)$$

With S closed, the SCE circuit is simplified to a $L_P - C_{T,\max}$ oscillator as shown in the left half of Fig. 3(b). Similar to the energy extraction process during State II+, energy is transferred to the primary inductor, followed by to the secondary inductor (when S is opened T_{SCE}^{I+} time later), and then to the battery load. During the time switch S is closed, the TENG capacitor discharges through the primary inductor, and hence $V_{C_T}(t)$ falls to zero. This resets TENG for the start of the next cycle (and State I+ ends)

$$V_T^{I+} = V_{\text{oc,min}} - V_{C_T}^{I+} = 0 - 0 = 0; \quad Q_{C_T}^{I+} = 0.$$

B. Percycle Energy Output

Cyclic TENG Voltage ($V_T(t)$) vs. TENG Capacitor Charge ($Q_{C_T}(t)$) diagram can be used to derive the percycle energy output (E_{cycle}) [11]

$$E_{\text{cycle}} = \int_0^T V_T I_T dt = \int_0^T V_T dQ_{C_T}. \quad (9)$$

Above equation shows that the energy output during the extraction step is equal to the area enclosed by the V_T curve against the Q_{C_T} axis. Using the TENG voltage (V_T) and capacitor charge (Q_{C_T}) derived at States I, I+, II, and II+ in the above section, the V_T versus Q_{C_T} plot for SCE is obtained as in Fig. 4(b). The first energy extraction step, at the end of the first half-cycle, II-II+, translates to a line with a slope of $-(C_{T,\min})^{-1}$ enclosing the area of region "1" in Fig. 4(b) equivalent to the extracted energy of E_{SCE}^{I}. While at the end of the second half-cycle, I-I+ step with a slope of $-(C_{T,\max})^{-1}$ extracts energy E_{SCE}^{II} equal to the area of region "2". The energy output found by computing the enclosed triangular areas of the regions "1" and "2" in Fig. 4(b) are stated as follows:

$$E_{\text{SCE}}^{I} = \frac{1}{2} \times C_{T,\min} V_{\text{oc,max}} \times V_{\text{oc,max}}$$

$$E_{\text{SCE}}^{II} = \frac{1}{2} \times C_{T,\min} V_{\text{oc,max}} \times \frac{V_{\text{oc,max}}}{\beta}$$

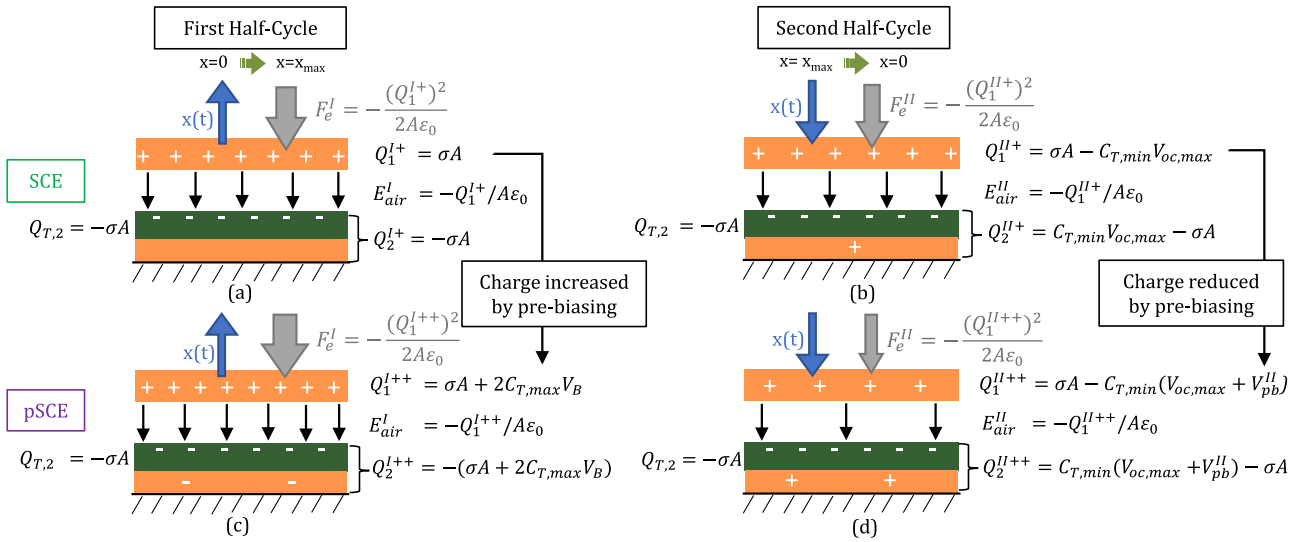

Fig. 5. TENG schematic depicting mechanical motion ($x(t)$) and electrostatic force (F_e) with the SCE circuit during (a) separation of TENG plates, i.e., first half-cycle and (b) retraction of the plates, i.e., second half-cycle. Comparative plots for the pSCE circuit during the (c) first half-cycle with relatively increased F_e and (d) second half-cycle with relatively reduced F_e.

$$E_{\text{SCE}} = E^{I}_{\text{SCE}} + E^{II}_{\text{SCE}} = \frac{1}{2}\left(1+\frac{1}{\beta}\right) C_{T,\min} V^2_{\text{oc,max}}. \tag{10}$$

Remark 1: The V_T versus Q_{C_T} plot for SCE cycle matches that of CMEO [11], [14]. Thus, all *passive* EECs i.e., without pre-biasing, are limited to the area enclosed by the SCE's V_T versus Q_{C_T} trapezoid, and in this sense, SCE is optimal among all the passive EECs. Also, SCE's energy output [see (10)] is independent of the load voltage value, which is another desirable feature eliminating the need for complex and power-intensive MPPT.

IV. Synchronous Pre-biasing for Enhanced Extraction

Synchronous pre-biasing refers to charging the TENG capacitor before the start of each half-cycle to possibly increase the energy output beyond the SCE output (CMEO). In this section, the electromechanical energy transduction at each step of the SCE circuit is first analyzed to motivate and quantify the effect of the proposed pre-biasing.

A. First Half-Cycle

For the SCE circuit, starting at State I+ ($x = 0$), the charge on the TENG capacitor is zero ($Q^{I+}_{C_T} = 0$). Hence, the charge on the TENG's upper plate (Q^{I+}_1) and the lower plate (Q^{I+}_2) are given by

$$Q^{I+}_1 = Q_{T,1} - Q^{I+}_{C_T} = \sigma A; \quad Q^{I+}_2 = -Q^{I+}_1 = -\sigma A. \tag{11}$$

In transitioning from State I+ ($x = 0$) to State II ($x = x_{\max}$), external mechanical excitation moves up the upper plate against the electrostatic force of attraction (F^I_e) acting on it [Refer Fig. 5(a)]. Noting that the electric field due to the bottom plate that acts on the charges of the upper plate is $\frac{1}{2}\vec{E}_\sigma$, using (1), we get

$$\vec{F}^I_e = \frac{1}{2}\vec{E}_\sigma Q^{I+}_1 = -\frac{1}{2}\left(\frac{\sigma}{\epsilon_0}\vec{1}_x\right)(\sigma A) = -\frac{1}{2}\left(\frac{\sigma^2 A}{\epsilon_0}\right)\vec{1}_x$$

$$W^I_e = \int_0^{x_{\max}} \vec{F}^I_e . d\vec{x} = -\frac{1}{2}\left(\frac{\sigma^2 A}{\epsilon_0}\right) x_{\max} = -\frac{1}{2}\left(\frac{(Q^{I+}_1)^2}{\epsilon_0 A}\right) x_{\max}$$

$$= -\frac{1}{2}\left(\frac{\beta}{\beta-1}\right) C_{T,\min} V^2_{\text{oc,max}} \tag{12}$$

where to derive the last equality, we use the defining equations of $C_{T,\min}$, $V_{\text{oc,max}}$, and β from Table I and (4), respectively. The work W^I_e done by the mechanical source (and stored as electrical potential energy) is proportional to the electrostatic force, which in turn is proportional to the square of the upper electrode charge ($(Q^{I+}_1)^2$). Thus, by pre-biasing (i.e., adding extra charge) the TENG at State I+, Q^{I+}_1 can be increased to in turn increase the transduced energy. This establishes the motivation behind pre-biasing, and in the following section, we quantify this energy gain for the proposed pSCE circuit.

Remark 2: It is clear that the transduced energy in the first half-cycle will continue to increase on increasing the pre-bias charge. In practice, the upper limit may be set by the level of available external mechanical force (equivalently acceleration). For a given periodic mechanical force with fixed acceleration, increasing the level of pre-biasing will increase the countering electrostatic force that will eventually reduce the maximum reachable separation between the two plates ($x_{\max}$) and, as a result, decrease the TENG's maximum open-circuit voltage ($V_{\text{oc,max}}$). This feedback effect of the electrostatic force in a vibration-driven electrostatic transducer on its mechanical motion and the transduced energy has been previously studied in works such as [33], [34]. In a typical TENG application with a moving part (upper plate in our case) of mass m, the deceleration due to electrical attraction (F_e/m) is an order or two lower in magnitude than the external mechanical acceleration. For example, human walking provides 2–3 ms^{-2} acceleration, while a car engine compartment provides 12 ms^{-2}[35]. In contrast, for the TENG used in this work (moving mass, $m = 113.7$ g), the

electrical deceleration is $0.013\ \text{ms}^{-2}$ with no pre-biasing (SCE operation) and $0.026\ \text{ms}^{-2}$ when pre-biased at 30 V as derived in Supplementary Note S.I. Thus, pre-biasing does not outpower the mechanical acceleration to cause an appreciable reduction in $x_{\max}$ value. Thereby in most mesoscale implementations, the pre-biasing level is limited only by the upper limit of the voltage source available for pre-biasing, the voltage ratings of the circuit components, or air electric field breakdown.

B. Second Half-Cycle

At the end of the first half-cycle, part of the transduced energy is extracted and delivered to the load (E^I_{SCE}), while part of it remains stored on the TENG capacitor. The charge on the upper plate at this stage, i.e., at State II+ (Q_1^{II+}) can be found using (6)

$$Q_1^{II+} = Q_{T,1} - Q_{C_T}^{II+} = \sigma A - C_{T,\min} V_{\text{oc,max}}. \tag{13}$$

With the start of the second half-cycle, as shown in Fig. 5(b), the direction of upper plate motion is reversed to match that of electrostatic force. This results in positive work, i.e., a part of stored TENG capacitor energy is dissipated back into the environment. This energy loss can be derived similarly to (12)

$$W_e^{II} = \frac{1}{2}\left(\frac{(Q_1^{II+})^2}{\epsilon_0 A}\right)x_{\max} = \frac{1}{2}\left(\frac{(\sigma A - C_{T,\min}V_{\text{oc,max}})^2}{\epsilon_0 A}\right)x_{\max}$$
$$= \frac{1}{2}\left(\frac{1}{\beta(\beta-1)}\right)C_{T,\min}V_{\text{oc,max}}^2. \tag{14}$$

In the entire cycle, the net work done (the work done in the first half cycle minus the energy lost in the second half cycle) is extracted. Indeed adding the above energy loss W_e^{II} [see (14)] to the extracted energy E_{SCE} [see (10)] gives us the transduced energy of the first cycle W_e^I [(12)]. Since, the three multipliers of the common term $\frac{1}{2}C_{T,\min}V_{\text{oc,max}}^2$ appearing in $W_e^{II}, E_{\text{SCE}}, W_e^I$ satisfy

$$\left(\frac{1}{\beta(\beta-1)}\right) + \left(1+\frac{1}{\beta}\right) = \left(\frac{\beta}{\beta-1}\right) \Rightarrow |W_e^{II} + E_{\text{SCE}}| = |W_e^I|$$

verifying the energy balance. We make a note that this the first time such an energy balance among the mechanical energy transduced, mechanical energy lost, and the electrical energy extracted for a TENG with SCE as EEC has been demonstrated to the best of our knowledge. For reducing the above energy loss to zero, the pre-biasing charge should be added to turn the plate charges ($Q_1^{II+} = -Q_2^{II+}$) to zero. Using (13)

$$Q_1^{II+} = 0 \Rightarrow \sigma A - C_{T,\min}V_{\text{oc,max}} - Q_{pb,\text{opt}}^{II} = 0$$
$$\Rightarrow V_{pb,\text{opt}}^{II} := \frac{Q_{pb,\text{opt}}^{II}}{C_{T,\min}} = \frac{\sigma A}{C_{T,\min}} - V_{\text{oc,max}}$$
$$\Rightarrow V_{pb,\text{opt}}^{II} = \frac{V_{\text{oc,max}}}{\beta - 1}. \tag{15}$$

However, pre-biasing voltage beyond twice the above derived optimum value ($V_{pb,\text{opt}}^{II}$) would decrease the upper plate charge below $-[\sigma A - C_{T,\min}V_{\text{oc,max}}]$, increasing the electrostatic attraction between the TENG plates beyond SCE, thereby causing a higher loss to the environment in the second half-cycle than that of SCE. Thus

$$V_{pb,u}^{II} := 2\,V_{pb,\text{opt}}^{11} = \frac{2V_{\text{oc,max}}}{\beta - 1} \tag{16}$$

provides the upper limit to pre-biasing in the second half cycle for it to remain favorable over SCE. In contrast, pre-biasing is always favorable in the first half-cycle and also overall, combining the two half-cycles, as demonstrated in the next section.

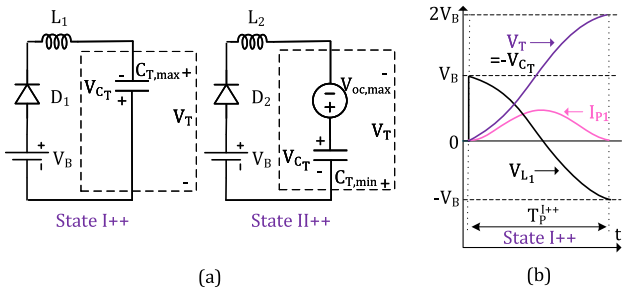

Fig. 6. pSCE circuit (a) Simplified circuit during pre-biasing at start of both the half-cycle and (b) L_1 inductor voltage (V_{L_1}), pre-biasing loop current (I_{P1}) and, TENG voltage (V_T) during pre-biasing State I++.

V. Proposed pSCE Circuit Analysis

Here, we describe the proposed circuit that is used for pre-biasing the TENG at the start of each half-cycle. To enable the same with either polarity, four additional switches S1–S4 configured as H-bridge are added to the SCE circuit architecture (see Fig. 2).

A. pSCE Operation

pSCE operation is obtained by extending the SCE operation discussed above with two added states for pre-biasing at the start of each half-cycle: State I++ (following I+) and State II++ (following II+). Circuit operation can be understood by following the operation cycle diagram of Fig. 7 and TENG voltage waveform of Fig. 4(a). As in SCE, the operation commences at $x = 0$, with all switches open and $V_{\text{oc}} = 0$ (State I+). Then for pre-biasing, switches S1 and S3 are closed (State I++ at the left top in Fig. 7) to form the pre-bias charging loop, $V_B - S_1 - L_1 - D_1 - C_T - S_3$ with the circuit simplified to a L_1-$C_{T,\max}$ oscillator as shown in the left half of Fig. 6(a). The corresponding circuit differential equation is similar to (5). The TENG capacitor voltage $V_{C_T}(t)$ with initial condition $V_{C_T}(0) = I_{C_T}(0) = 0$ is obtained as,

$$V_{C_T}(t) = V_B(\cos(\omega_P^{I++}t)) - V_B; \quad \omega_P^{I++} = \frac{1}{\sqrt{L_1 C_{T,\max}}}.$$

On enabling S1 and S3 for half the oscillation cycle (denoted T_P^{I++}), the TENG capacitor voltage reaches $-2V_B$

$$V_{C_T}^{I++} := V_{C_T}\left(\frac{\pi}{\omega_P^{I++}}\right) = V_{C_T}\left(T_P^{I++}\right) = -2V_B.$$

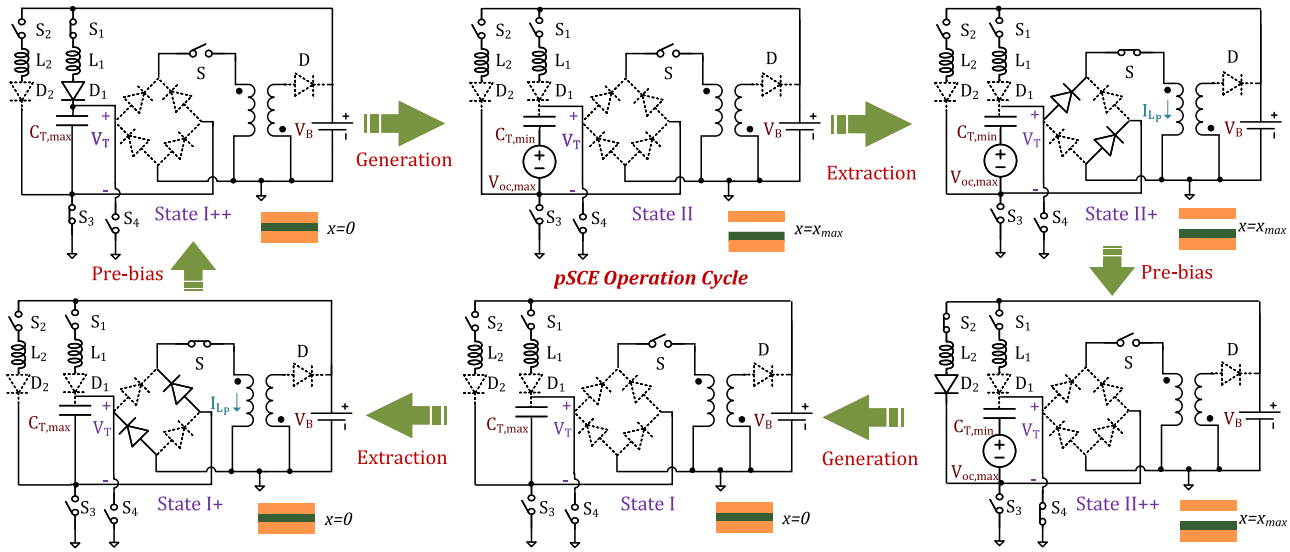

Fig. 7. Proposed pSCE circuit's operation cycle.

Using the TENG operating equation [see (3)], with $V_{\text{oc}} = 0$

$$V_T^{I++} = -\frac{Q_{C_T}^{I++}}{C_{T,\max}} = 2V_B \Rightarrow Q_{C_T}^{I++} = -2C_{T,\max}V_B. \quad (17)$$

Thus, using the L_1-C_T resonance, the pre-biasing voltage is passively boosted to twice the pre-biasing source (battery) voltage by introducing the extra inductor L_1 (correspondingly L_2 for the second half-cycle). At this point, the two plates separate with switch S open, and TENG voltage increases to reach its maxima at State II. As no current has flown through TENG since the last state, $Q_{C_T}^{II} = Q_{C_T}^{I++}$. Hence

$$V_T^{II} = V_{\text{oc,max}} - \frac{Q_{C_T}^{II}}{C_{T,\text{min}}} = V_{\text{oc,max}} + 2\beta V_B. \quad (18)$$

Note the increase in the voltage by $2\beta V_B$ compared to the SCE circuit. At this stage, similar to the SCE circuit, switch S is closed for one-fourth the L_P-$C_{T,\text{min}}$ oscillation cycle (T_{SCE}^{II+}) to achieve State II+. TENG voltage falls to zero, and the energy is transferred to the primary inductor L_p, which is subsequently transferred to the load via secondary inductor L_S. With the first half-cycle complete, similar to the State I++ operation, the State II++ operation is performed to pre-bias the TENG by closing S2 and S4 (right bottom in Fig. 7) to form the $V_B - S_2 - L_2 - D_2 - C_T - S_4$ loop, with the circuit simplified to a L_2-$C_{T,\text{min}}$ oscillator as shown in the right half of Fig. 6(a). With initial conditions: $V_{C_T}(0) = V_{\text{oc,max}}$; $I_{C_T}(0) = 0$, the TENG capacitor satisfies

$$V_{C_T}(t) = V_B(1 - \cos(\omega_P^{II++}t)) + V_{\text{oc,max}}$$
$$\omega_P^{II++} = \frac{1}{\sqrt{L_2 C_{T,\text{min}}}}.$$

Since $V_{C_T}(t)$ oscillates between $V_{\text{oc,max}}$ and $V_{\text{oc,max}} + 2V_B$, the TENG voltage $V_T(t) = V_{\text{oc,max}} - V_{C_T}(t)$ oscillates between 0 and $-2V_B$. Thus, by controlling the duration over which S2 and S4 are closed, i.e., the duration of pre-biasing, the TENG voltage can be set to any value $-V_{pb}^{II}$ such that $-2V_B \leq -V_{pb}^{II} \leq 0$ (Refer Supplementary Note S.II at for further explanation). Then

$$V_T^{II++} = V_{\text{oc,max}} - \frac{Q_{C_T}^{II++}}{C_{T,\text{min}}} = -V_{pb}^{II}$$
$$\Rightarrow Q_{C_T}^{II++} = C_{T,\text{min}}(V_{\text{oc,max}} + V_{pb}^{II}). \quad (19)$$

Next, as per the periodic motion, the plates come together ($x = 0$) as in State I. Since the TENG is in open-circuit condition during this movement, $Q_{C_T}^{I} = Q_{C_T}^{II++}$. Hence

$$V_T^{I} = -\frac{Q_{C_T}^{I}}{C_{T,\max}} = -\frac{V_{\text{oc,max}} + V_{pb}^{II}}{\beta}. \quad (20)$$

Again, at this stage, the TENG voltage is higher (in absolute terms) over the SCE circuit [see (7)], meaning larger energy will be recovered in going from State I to State I+. Next, the switch S is closed for one-fourth the L_p-$C_{T,\max}$ oscillation cycle, i.e., for T_{SCE}^{I+} to extract the energy from TENG (State I+ at the left bottom in Fig. 7). TENG voltage falls to zero, completing one full operation cycle.

B. Percycle Energy Output

As with the case of SCE percycle energy output calculation, we plot the TENG voltage (V_T) and TENG capacitor charge (Q_{C_T}), derived above, at different states to obtain the V_T-Q_{C_T} plot of Fig. 4(b). Note due to pre-biasing, the trapezoidal area of SCE extends on both sides (beyond the regions labeled "1" and "2" of SCE), adding the regions labeled as "3," "4," "5," and "6." The pre-biasing adds charge $-2C_{T,\max}V_B$ raising TENG voltage to $2V_B$ during State I++ [see (17)], while during State II++ adds charge $C_{T,\text{min}}V_{pb}^{II}$ lowering TENG voltage to $-V_{pb}^{II}$ [see (19)]. As a result, the energy extracted at the end of the first half-cycle (E_{pSCE}^{I}) is equal to the triangular area enclosed by the extraction step, namely, State II to II+ line, and the Q_{C_T} axis (areas "1"+"3"+"4"). Similarly, energy extracted at the end of the second half cycle (E_{pSCE}^{II}) is the triangular area between

State I to I+ line and the Q_{C_T} axis (areas "2"+"5"+"6")

$$E^{I}_{\text{pSCE}} = \frac{1}{2}\times C_{T,\min}(V_{oc,max}+2\beta V_B)\times(V_{\text{oc,max}}+2\beta V_B);$$

$$E^{II}_{pSCE} = \frac{1}{2}\times C_{T,\min}(V_{\text{oc,max}}+V^{II}_{pb})\times\frac{(V_{\text{oc,max}}+V^{II}_{pb})}{\beta}. \quad (21)$$

The energy consumed from the load battery for the TENG pre-biasing at the start of each half-cycle is equal to the product of the battery voltage and the charge flow during the pre-biasing periods. The consumed pre-biasing energy for the first half-cycle ($E^{I}_{\text{pre-bias}}$) and that for the second half-cycle ($E^{II}_{\text{pre-bias}}$) are thus, respectively, equal to the areas marked as "3" and "5" on the V_T-Q_{C_T} plot of Fig. 4(b)

$$E^{I}_{\text{pre-bias}} = 2C_{T,\text{max}}V_B^2 = 2\beta C_{T,\min}V_B^2$$

$$E^{II}_{\text{pre-bias}} = \frac{1}{2}C_{T,\min}(V^{II}_{pb})^2. \quad (22)$$

Since the total extracted energy is the sum of areas "1" through "6," it can be said that the "invested energy" of "3"+"5" is recouped with a "return on investment" (in addition to the SCE output of "1"+"2") as "4"+"6." Now, individually, the net energy delivered to the battery load in the two half-cycles obtained by deducting the respective pre-biasing energy from the extracted energy can be expressed as

$$E^{I}_{\text{pSCE,net}} = \frac{1}{2}C_{T,\min}\left[(V_{\text{oc,max}}+2\beta V_B)^2 - 4\beta V_B^2\right]$$

$$E^{II}_{\text{pSCE,net}} = \frac{1}{2}C_{T,\min}\left[\frac{\left(V_{\text{oc,max}}+V^{II}_{pb}\right)^2}{\beta} - (V^{II}_{pb})^2\right]. \quad (23)$$

Sum of the above two equals the area enclosed by the pSCE operation (regions "4"+"1"+"2"+"6") on the V_T-Q_{C_T} plot of Fig. 4(b) and represents the net percycle energy extracted from TENG

$$E_{\text{pSCE,net}} = \frac{1}{2}C_{T,\min}\left[(V_{\text{oc,max}}+2\beta V_B)^2 + \frac{\left(V_{\text{oc,max}}+V^{II}_{pb}\right)^2}{\beta} - 4\beta V_B^2 - \left(V^{II}_{pb}\right)^2\right]. \quad (24)$$

C. Conditions for Pre-biasing

For the first half-cycle, *Remark 2* above discussed that compared to the SCE operation, pre-biasing increases the transduced energy which can now be verified from energy point of view by showing that $E^{I}_{\text{pSCE,net}}$ at any arbitrary pre-biasing voltage [substituting V^{I}_{pb} for $2V_B$ in (23)] is greater than E^{I}_{SCE} [see (10)] and continues to increase with V^{I}_{pb}

$$E^{I}_{\text{pSCE,net}} - E^{I}_{\text{SCE}} \geq 0$$
$$\Leftrightarrow \left[(V_{\text{oc,max}}+\beta V^{I}_{pb})^2 - \beta(V^{I}_{pb})^2\right] - V^2_{\text{oc,max}} \geq 0$$
$$\Leftrightarrow \beta\left[2V_{\text{oc,max}} + (\beta-1)V^{I}_{pb}\right]V^{I}_{pb} \geq 0.$$

Since $\beta \geq 1$, the above inequality clearly holds, where the left-hand side is an increasing function of V^{I}_{pb} (higher the pre-biasing; higher the gain).

For the second half-cycle, we noted in Section IV-B that pre-biasing beyond a limit increases the energy loss to the environment, so it becomes higher than the corresponding energy loss of SCE. The same limit on the load voltage, beyond which it is preferable to skip pre-biasing for the second half-cycle, can be derived by way of energy considerations

$$E^{II}_{\text{pSCE,net}} - E^{II}_{\text{SCE}} \geq 0$$
$$\Leftrightarrow \left[\frac{(V_{\text{oc,max}}+V^{II}_{pb})^2}{\beta} - (V^{II}_{pb})^2\right] - \frac{V^2_{\text{oc,max}}}{\beta} \geq 0$$
$$\Leftrightarrow 2V_{\text{oc,max}} - (\beta-1)V^{II}_{pb} \geq 0$$
$$\Leftrightarrow V^{II}_{pb} \leq \frac{2V_{\text{oc,max}}}{(\beta-1)} =: V^{II}_{pb,u}. \quad (25)$$

This condition obtained based on energy considerations matches the condition of (16) that was derived using the level of charge on the two plates (and the corresponding level of electrostatic attraction), providing a correctness check to our derivations. Differentiating the above gain of pSCE circuit over SCE in the second half-cycle ($E^{II}_{\text{pSCE,net}} - E^{II}_{\text{SCE}}$) with respect to V^{II}_{pb} and equating it to zero provides the optimum level of pre-biasing as

$$V^{II}_{pb,\text{opt}} = \frac{V_{\text{oc,max}}}{(\beta-1)} \quad (26)$$

which is again consistent with the result of (15) derived from the charges/forces perspective in Section IV-B.

Another novel result can be deduced by mapping the derived optimal battery voltage value $V^{II}_{pb,\text{opt}}$ to the TENG parameters

$$V^{II}_{pb,\text{opt}} = \frac{V_{\text{oc,max}}}{\beta-1} = \frac{\frac{\sigma x_{\max}}{\epsilon_0}}{\frac{x_{\max}+d_{\text{eff}}}{d_{\text{eff}}}-1} = \frac{\sigma d_{\text{eff}}}{\epsilon_0}$$

a constant value for a given TENG. This implies that the optimal load voltage $V^{II}_{pb,\text{opt}}$ does not depend on the operation parameters such as amplitude ($x_{\max}$) or operation frequency, and as such, no dynamic closed-loop control is required to adjust the pre-biasing voltage for optimized pSCE operation.

Remark 3: Since $V^{II}_{pb,\text{opt}} < V^{II}_{pb,u}$ (the former is the half of the latter), it follows that it is favorable to operate at the optimum pre-bias level of $V^{II}_{pb,\text{opt}}$ in the second half cycle whenever it is feasible. So, if $V^{II}_{pb,\text{opt}} \leq 2V_B$, then in the second half cycle, one would pre-bias the TENG to the voltage $-V^{II}_{pb,\text{opt}}$ by appropriately controlling the on-time of the switches S2 and S4 (note as discussed just prior to eq. (19), it is possible to pre-bias the TENG voltage to as low as $-2V_B$). On the other hand, in the suboptimal case of $2V_B < V^{II}_{pb,\text{opt}}$, the best one can do in the second half cycle from the energy perspective is to pre-bias the TENG to the voltage $-2V_B$. We next show that even in the suboptimal operation of the second half cycle (namely, pre-biasing TENG voltage to $-2V_B$ in all cases), the net energy gain of pSCE over SCE in the combined two half-cycles is positive for any V_B value. This can be seen from the following sequence of

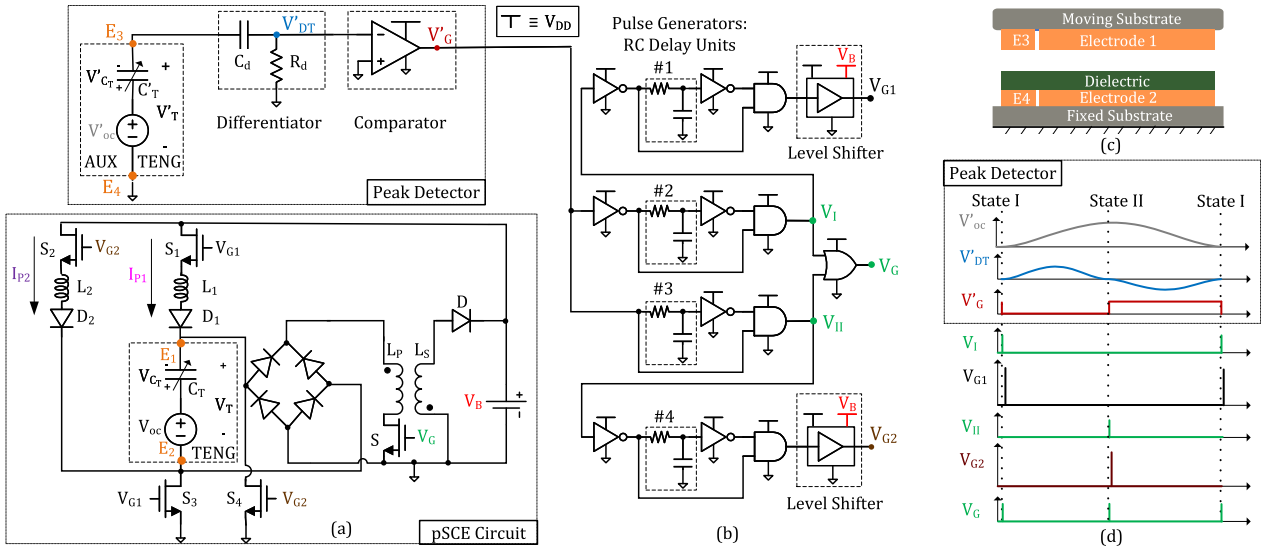

Fig. 8. (a) pSCE circuit implementation. (b) Control circuit with peak detector and four pulse generators. (c) Cross-section diagram of TENG showing parallel isolated Aux-TENG. (d) Schematic of control circuit waveforms.

equivalences:

$$\left[E_{\text{pSCE,net}}|_{V_{pb}^{II}=2V_B}\right] - E_{\text{SCE}} \geq 0$$

$$\Leftrightarrow (V_{\text{oc,max}} + 2\beta V_B)^2 + \frac{(V_{\text{oc,max}} + 2V_B)^2}{\beta}$$

$$- 4(1+\beta)V_B^2 - \left(1 + \frac{1}{\beta}\right) V_{\text{oc,max}}^2 \geq 0$$

$$\Leftrightarrow \left(\beta + \frac{1}{\beta}\right) V_{\text{oc,max}} + (\beta - 1)\left(\beta - \frac{1}{\beta}\right) V_B \geq 0. \quad (27)$$

By definition, $\beta \geq 1$ and thus, the above condition is satisfied at all load values for any given TENG. Also, in the final inequality of (27), the left-hand side is an increasing function of V_B, implying that the energy gain of the pSCE circuit over the SCE circuit shall continue to rise with increasing value of V_B. Thus, barring an eventual reduction in $x_{\max}$ due to the increased pre-biasing or air electric field breakdown (as discussed earlier in *Remark 2*), there is no other upper limit on V_B as far as being able to boost the energy output through pre-biasing. Pre-biasing to a level higher than the presented design's upper limit of twice the battery voltage ($\pm 2V_B$) is also possible, but only at the added energy cost of dc/dc boosting. It is an easy exercise to check if the *net* energy gain by introducing such a boosted pre-biasing would be positive for a given TENG, and if so, a dc/dc boost can be integrated if the application can afford its added area.

Remark 4: While our paper proposes and derives results for pre-biasing the TENG operating in the generic contact-separation mode, the results are also valid for the lateral sliding mode TENG, which has similar time-varying capacitance and open-circuit voltage characteristics [2]. However, for the free-standing mode TENG, wherein a dielectric plate oscillates in the air-gap of two stationary metal electrodes, the capacitance is fixed and hence $\beta = 1$ [2]. In this case, both the half-cycles (upward and downward stroke of the dielectric plate) are symmetric and both transduce energy from the mechanical source and in that sense, are similar to the above described contact-separation mode TENG's first half-cycle. Thus, in line with *Remark 2*, synchronous pre-biasing can also be used for the freestanding mode TENG to increase the net energy extracted, and as such, no upper limit exists on the level of pre-biasing (other than that imposed by the breakdown voltage of the operating medium).

VI. Circuit Implementation

The proposed pSCE circuit's implementation with MOSFET switches is shown in Fig. 8(a). The SCE circuit is implemented in a similar fashion, minus the H-bridge portion of the pSCE.

A. Switching Controller

The pSCE circuit operates by switching at the extrema (States I and II), with the NMOS switches receiving the signal from the control circuit. Fig. 8(b) shows the control circuit that comprises of a peak detector and four pulse generators that issues gate pulse V_G for switching S and achieving the energy extraction States I+ and II+, V_{G1} for switching S1 and S3 and achieving pre-biasing State I++, and V_{G2} for switching S2 and S4 and achieving pre-biasing State II++.

The peak detector identifies the operation extrema by tracking the output voltage of an electrically isolated auxiliary TENG (Aux-TENG) built with a fraction of area compared to the main TENG that operates synchronously in parallel to the main TENG as schematized in Fig. 8(c). The output voltage V_T' of Aux-TENG is differentiated by the CR circuit (V_{DT}'), to convert the signal peaks into zero crossings, which trigger state change of the comparator output V_G', at States I and II as schematized in Fig. 8(d). Independent Aux-TENG is used as an input for the control circuit as opposed to the rectified voltage of the main TENG to be able to distinguish State I from State II and accordingly set the switching time T_{SCE}^{I+} or T_{SCE}^{II+} [see (8)] for switch S, and additionally enable either pair of switches (S1,S3)

or (S2,S4) to pre-bias the TENG with the correct polarity. Use of Aux-TENG also avoids loading of the main TENG by the control circuit and subsequent interference.

Further, four pulse generating arms of the circuit are designed to generate a pulse at the rising edge of the input: Arm 3 receives the comparator output and generates a pulse at State II (V_{II}). Similarly, Arm 2 generates the pulse at State I (V_I) on receiving the inverted comparator output. The pulse width is set by the *RC* product of the respective delay unit. It is set to T_{SCE}^{I+} and T_{SCE}^{II+} for the Arms 2 and 3, respectively. Both these signals are combined through OR gate to produce signal V_G for the NMOS S. Arm 1 is used to generate a pulse for switching on NMOS S1 and S3 (V_{G1}) at the falling edge of the signal V_I for the follow-up pre-biasing of State I++. The source of S1 reaches voltage upto V_B by the end of the pre-biasing action, hence to keep it turned ON, the signal (V_{G1}) is shifted up from control circuit supply voltage V_{DD} to V_B using the voltage level shifter. The pulse width of this signal should be greater than or equal to half the L_1-$C_{T,\max}$ resonator cycle (T_P^{I++}) to complete the pre-biasing action. At the end of the half-cycle, the current direction reverses and is automatically cut-off due to diode D_1 in the loop. Similarly, V_{G2} is generated using Arm 4 to switch on NMOS S2 and S4 for the pre-biasing step of State II++. Note that the SCE circuit too operates with the same switching controller of Fig. 8(a) barring the Arms 3 and 4 of the circuit.

1) Control Circuit Delay: Here we quantify the control circuit's time delay in detecting the TENG operation extremes, and show how it is orders of magnitude lower than the TENG's operation cycle time and hence has a negligible impact on its overall performance. The consequential source of delay is the peak detector's CR differentiator, introducing a quarter-cycle delay to attain the zero crossings at States I and II. Referring to the circuit of Fig. 8(b), the Aux-TENG is connected in series with resistor R_d and a small valued capacitor C_d (of the order of 1 pF) compared to the minimum Aux-TENG capacitance rendering the effective series capacitance as $\sim C_d$. The amplitude ($|V'_{DT}|$) and phase (θ) of the voltage across R_d that is input to the comparator can be derived as:

$$|V'_{DT}| = \left(\frac{V'_{\text{oc,max}}}{2}R_d\right)\frac{\omega_{\text{ext}}C_d}{\sqrt{1+(\omega_{\text{ext}}R_dC_d)^2}}$$
$$\theta = \arctan\left(\frac{1}{\omega_{\text{ext}}R_dC_d}\right) = \frac{\pi}{2} - \arctan\left(\omega_{\text{ext}}R_dC_d\right). \tag{28}$$

Here, ω_{ext} is the external (mechanical) operation frequency. The offset $\arctan(\omega_{\text{ext}}R_dC_d)$ to $\pi/2$ in θ is the undesirable delay that can be written in time difference/delay (t_d) form as

$$t_d = \frac{\arctan(\omega_{\text{ext}}R_dC_d)}{\omega_{\text{ext}}} \approx R_dC_d.$$

Clearly, this delay can be minimized by reducing the R_dC_d product. With a typical choice of C_d =1 pF, a R_d of the order of 100 M Ω is sufficient to produce large enough output ($|V'_{DT}| \propto V'_{\text{oc,max}}R_dC_d$ by (28)) to trigger the zero-crossing in the comparator. The above choice translates to a delay of the order of $\sim 10\,\mu$s that is negligible compared to TENG operating time period (100 ms corresponding to operation frequency of 10 Hz for this work). The propagation delay added by the comparator and other logic gates is again of the order of a few μs. Thus, the control circuit's time delay is safely ignored for analysis purposes.

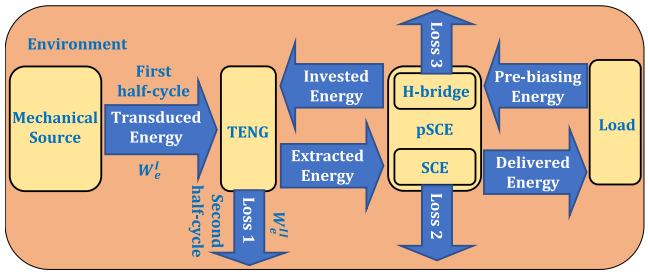

Fig. 9. Energy flow diagram for the pSCE operation. Loss 1 is electrostatic environmental loss while Loss 2 and 3 are parasitic conduction losses.

B. Impact of Circuit Nonidealities

In practical implementation of the SCE/pSCE circuit, different circuit parasitic losses impact the energy delivered to the load as computed using the $V_T - Q_{C_T}$ plot in the above sections, which we describe next.

1) Conduction Loss: First, in the SCE circuit, the resistive losses occur due to the series parasitic inductor resistance and the ON-state resistance of switch S, during the two energy extraction steps of States I+ and II+. The full derivation of per-cycle energy delivered to the load with consideration of the resistive loss is provided in Supplementary Note S.III. In brief, this loss due to cumulative series resistance, denoted R_S, can be modeled by defining the series quality factor (Q_f) of the L_PC_T resonator loops formed by closing switch S for energy extraction. For convenience, we use the "normalized" forms $0 < \alpha^I < 1$ and $0 < \alpha^{II} < 1$ of the quality factors during State I+ and II+, respectively, as defined below:

$$\alpha^I := e^{\frac{-\pi}{2Q_f^I}}; Q_f^I := \frac{\omega_d^I L_P}{R_S}, \omega_d^I := \sqrt{\frac{1}{L_PC_{T,\max}} - \frac{R_S^2}{4L_P^2}}$$
$$\alpha^{II} := e^{\frac{-\pi}{2Q_f^{II}}}; Q_f^{II} := \frac{\omega_d^{II} L_P}{R_S}, \omega_d^{II} := \sqrt{\frac{1}{L_PC_{T,\min}} - \frac{R_S^2}{4L_P^2}}.$$

Now, the percycle energy delivered to the load can be stated as [see (S6) of Supplementary Note S.III]:

$$E_{\text{SCE}} = \frac{1}{2}\left(\frac{\alpha^I}{\beta} + \alpha^{II}\right)C_{T,\min}V_{\text{oc,max}}^2.$$

Here, while the two diode voltage drops ($2V_D$) in the FWR of the SCE circuit has been ignored due to high voltage nature of the TENG, it can be easily incorporated in the derivation.

Note since the SCE circuit acts as the extraction circuit in the pSCE operation, the conduction loss of pSCE during the energy extraction steps (marked as "Loss 2" in the energy flow diagram of Fig. 9) can be modeled similar to the SCE circuit already presented above. The additional losses in the two pre-biasing paths of $S_1 - L_1 - S_3$ and $S_2 - L_2 - S_4$ ("Loss 3" in Fig. 9) need

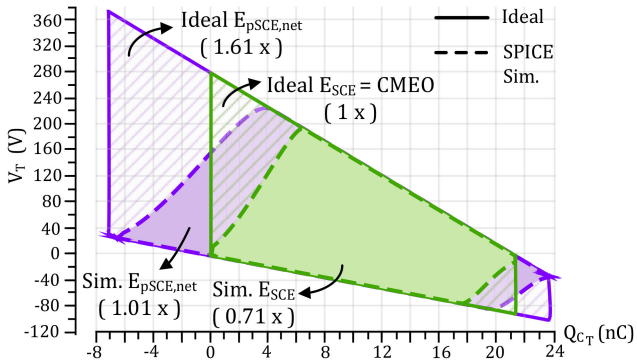

Fig. 10. Ideal and simulated TENG voltage vs. charge plot for the SCE and pSCE circuits at 15 V load. Enclosed area represents the net energy extracted from one operation cycle of TENG.

to be incorporated as well. Letting $L_1 = L_2 = L_P$ so that the quality factor of the pre-biasing loops $L_1 C_{T,\max}$ and $L_2 C_{T,\min}$ are also α^I and α^{II} during States I++ and II++, respectively, the percycle energy delivered to the load V_B using pSCE circuit can be stated as [see (S11) of Supplementary Note S.IV]:

$$E_{\text{pSCE,net}} = \frac{1}{2} C_{T,\min} \Bigg[(\alpha^{II}) \left(V_{\text{oc,max}} + (1+\alpha^I)\beta V_B \right)^2 + \frac{(\alpha^I) \left(V_{\text{oc,max}} + (1+\alpha^{II}) V_B \right)^2}{\beta} - 2 \left(1 + \alpha^{II} + (1+\alpha^I)\beta \right) V_B^2 \Bigg] \tag{29}$$

for the case, where the TENG is pre-biased for half the LC_T resonator cycle, i.e., upto the maximum achievable voltage during both States I++ and II++.

2) Leakage Current Loss: Both the SCE and pSCE circuits operate with switches off most of the time (barring the short duration at States I and II), and the leakage of charge through the nonideal MOSFET switches and the reverse biased diodes of the FWR results in lower voltage magnitudes at States I and II and hence, lower extracted energy. The leakage current changes dynamically as the TENG voltage varies during the operation cycle and is also governed by the nonideal characteristics of diodes and MOSFETs. To understand the effect of leakage on energy extraction, we take the aid of simulation using SPICE models of the diodes and MOSFETs used in the experimental implementation of this work (The list of these off-the-shelf components is provided in Supplementary Note S.V). Consider the simulated circuit operation (plotted in dotted lines) for the SCE and pSCE circuits at 15 V load in the form of TENG voltage versus charge ($V_T - Q_{C_T}$) plot of Fig. 10: It can be observed that leakage alters the operation contour from the envisaged ideal operation contour (coplotted using solid lines), reducing the enclosed area or equivalently the net extracted energy. In case, the estimate of leakage charges (that depends on TENG voltage as well as switch and diode characteristics) during the switch OFF-times are available, the percycle energy results can be revised, e.g., in the SCE circuit, the voltage at State II, $V_T^{II} = V_{\text{oc,max}}$ will be revised to $V_{\text{oc,max}} - (C_{T,\min} Q_L^I)$, where Q_L^I is the leakage charge in the first half-cycle.

For the TENG with parameters of Table II, the ideal net percycle energy output of the pSCE circuit at 15 V load as per the area enclosed by $V_T - Q_{C_T}$ plot is 6.34 μJ or 1.61 times the CMEO, as marked in Fig. 10. In contrast, the simulation shows the net extracted energy to be 3.96 μJ. Finally, the net energy delivered to the load is further reduced to 2.51 μJ due to conduction losses during energy extraction and pre-biasing steps. While there would be other losses such as parasitic losses due to nonideal coupling in the transformer, these results already closely match the ones experimentally observed.

TABLE II
MEASURED TENG PARAMETERS

Maximum open-circuit voltage: $V_{\text{oc,max}}$	279.92 V
Minimum TENG capacitance: $C_{T,\min}$	75.97 pF
Maximum TENG capacitance: $C_{T,\max}$	239.23 pF
TENG capacitance ratio: β	3.15

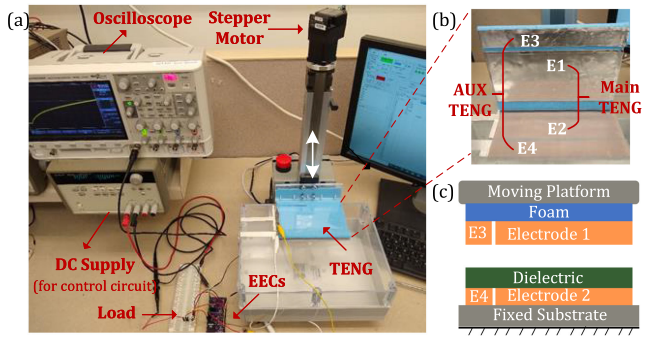

Fig. 11. (a) Experimental Setup. (b) Disassembled view of TENG. (c) Schematic cross-section diagram of the implemented TENG.

VII. EXPERIMENTAL IMPLEMENTATION

A. Experimental Setup

The overall experimental setup is shown in Fig. 11(a). TENG with a contact area of 112.5 cm ^{2} is implemented as in the schematic of Fig. 11(c). The fixed bottom plate is made of Teflon (dielectric) of thickness 127 μ m on top of an Al sheet (electrode). The upper plate with the Al sheet (electrode) is driven in a reciprocating fashion by a stepper motor (Applied Motion STM 17Q-3AE) programmed using vendor-provided software (Q Programmer) at 10 Hz frequency, with an amplitude ($x_{\max}$) of 1.64 mm. An electrically isolated auxiliary TENG (Aux-TENG) with 1/5th the main TENG area is created to operate synchronously in parallel [a blow-up of the same is shown in Fig. 11(b)], and is tapped using electrodes 3 and 4 to provide the input signal to the control circuit, issuing switching pulses to the SCE/pSCE circuits in synchrony with the main TENG. Fig. 11(a) also shows the implemented EEC and load. Output is measured using the oscilloscope (Keysight DSOX2024 A) and the data is collected through the NI's data acquisition card and labview program. The dc supply powers the control circuit so that the energy

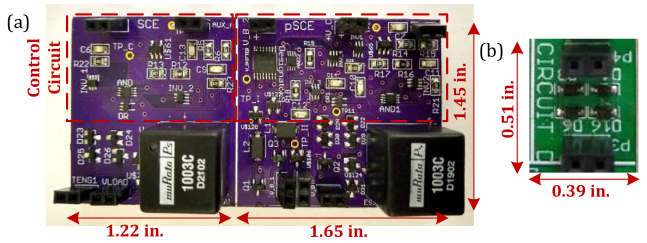

Fig. 12. PCB implementations of the (a) SCE circuit, pSCE circuit, and (b) FWR circuit.

consumed by the control circuits of SCE/pSCE can be measured noninterferingly.

B. TENG Characterization

TENG is characterized by the three main parameters: minimum and maximum TENG capacitance ($C_{T,\text{min}}$ and $C_{T,\text{max}}$), and maximum open-circuit voltage ($V_{\text{oc,max}}$), that are summarized in Table II for our experimental TENG. Dynamic variation of TENG capacitance is measured using the phase response based method described in [28] and is plotted in Fig. S3 of Supplementary Note S.VI from which the maximum and minimum values of the TENG capacitor are obtained. On the other hand, the maximum open-circuit voltage is measured with the aid of the FWR circuit as in [24], with details provided in Supplementary Note S.VII.

C. Implementation

Both the pSCE circuit and its switching controller are implemented as per Fig. 8 using off-the-shelf components over a PCB as shown in Fig. 12(a). Additionally, SCE and the standard FWR circuits are implemented over PCB [shown in Fig. 12(a) and (b), respectively] for performance comparison with the proposed pSCE circuit. As mentioned earlier, the SCE circuit is implemented similar to the pSCE circuit, barring the H-bridge and the control circuit's Arms 1 and 4 (refer Fig. 8) and same transformer with turns ratio 2:1 (refer Supplementary Table S1 is used for both the circuits. The control circuit of both the SCE and pSCE circuits are powered at voltage V_{DD} of 3 V with their percycle control circuit consumption measured as $0.293\ \mu$J and $0.423\ \mu$J (at $V_B = 10\,V$), respectively. It should be noted that for our validation experiments, off-the-shelf components are used to implement the control circuit as a proof-of-study. Hence, there is a large room for further optimization to reduce this consumption, for example, by using a custom-designed IC. The extraction circuits have been designed to have the onboard load battery also supply the power needed for the switching actions of both SCE and pSCE operations. In case a cold-start is needed, the battery charging can first start in the passive FWR mode, requiring no switching energy (as for example in [19]), and once sufficient energy for SCE/pSCE action has been accumulated, the switch to SCE/pSCE operation can initiate. Note that the battery voltage needs to rise above the H-bridge path's threshold voltage of one diode and two switches, typically $\sim$2 V, for the pSCE action to start.

VIII. Results and Discussion

Given $V_{\text{oc,max}} = 279.92$ V and $\beta = 3.15$ (see Table II), optimum pre-biasing voltage in second half-cycle ($V^{II}_{pb,\text{opt}}$) is calculated to be 130.19 V. Since we employ battery load of at most $16\,V$ for testing, in our experiments it holds that $2V_B \leq V^{II}_{pb,\text{opt}}$, and so following *Remark 3*, we pre-bias to $-2V_B$ at State II++ (The pre-biasing at State I++ is always at the maximum possible level of $2V_B$). The measured TENG voltage (V_T), secondary inductor (load) current (I_{L_S}), and the control voltage (V_G) waveforms for the pSCE circuit at $10\,V$ battery load are shown in the center of Fig. 13. The two zoomed-in views at States I and II show the rising primary inductor current (I_{L_P}) as the switch S is enabled by V_G for energy extraction, which is followed by the rise of secondary inductor current (I_{L_S}) as triggered by the fall of signal V_G (NMOS S turns OFF). The zoomed-in views at States I and II also show the measured pre-biasing control signal, V_{G1} (resp., V_{G2}), triggered by the fall of V_G, and the pre-biasing current, I_{P1} that flows through the V_B-S_1-L_1-D_1-C_T-S_3 (resp., I_{P2} through V_B-S_2-L_2-D_2-C_T-S_4) path. Fig. 14 plots the measured periodic TENG voltage waveforms, $V_T(t)$ for the pSCE circuit with load voltage V_B as 5, 10, 15 V along with the SCE circuit (as a base case). In line with the derivations above, the pSCE circuit, pre-biased with twice the battery load ($|2V_B|$), shows increasingly higher TENG voltage magnitudes at both States I and II with rising load battery voltage V_B and is always higher than its SCE counterpart as observed from Fig. 14. This contributes to pSCE's increased percycle energy output as quantified in the following.

A. Comparison With FWR and SCE Circuits

The fundamental comparison of the first time presented pSCE circuit is with its peer SCE circuit, together with the base case FWR circuit. For our experimental TENG with the parameters listed in Table II, the measured percycle energy output (E_{cycle}) using FWR, SCE, and pSCE circuit as EECs against battery loads are compared in Fig. 15. It is calculated as the product of load voltage (V_B) and integration of the measured current (charge) flowing through the load battery over one cycle. For the pSCE circuit, the net percycle energy ($E_{\text{pSCE,net}}$) is plotted, which is obtained by deducting the pre-biasing energy ($E_{\text{pre-bias}}$: calculated as the product of V_B and the integration of pre-biasing current, I_P over one cycle) from the gross output energy (E_{pSCE}).

As evident from Fig. 15, E_{cycle} for FWR shows the expected parabolic response with variation in load voltage [10], [24]. SCE circuit has a constant energy output irrespective of V_B as expected from the circuit analysis in Sec. III and confirming *Remark 1*. For the pSCE circuit, an increasing net energy output trend is observed with the increasing value of V_B validating the theoretical development in Section V. Table III lists the gain of the pSCE circuit over SCE and FWR circuit at three different load voltages. The pSCE circuit's gain increases with higher pre-biasing through the battery as the SCE output remains constant. Initially, the gain over FWR decreases with rising V_B due to the parabolic nature of FWR's E_{cycle} but is expected to rise later at higher V_B. Further, the power density figures of FWR, SCE, and pSCE circuits from our experimental implementation

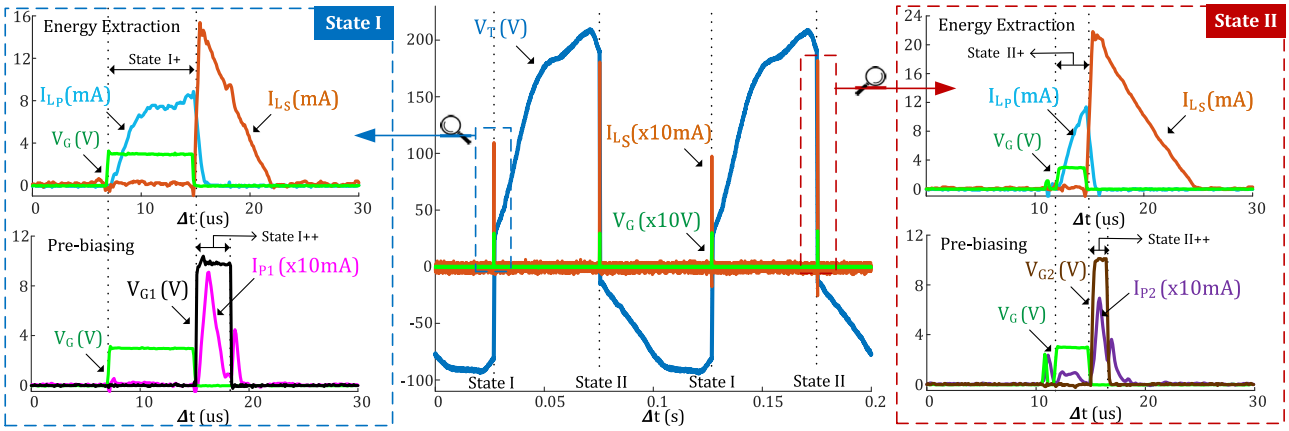

Fig. 13. Measured TENG Voltage V_T, secondary inductor (load) current I_{L_S}, and the control signal V_G for the switch S over two operation cycles of the pSCE circuit at 10 V battery load. Additionally, the zoomed-in views at States I and II plot the primary inductor current I_{L_P} during the energy extraction step of State I+ (resp., State II+), the control signal V_{G1} for S1 and S3 (resp., V_{G2} for S2 and S4), pre-biasing current I_{P1} (resp., I_{P2}) during State I++ (resp., State II++).

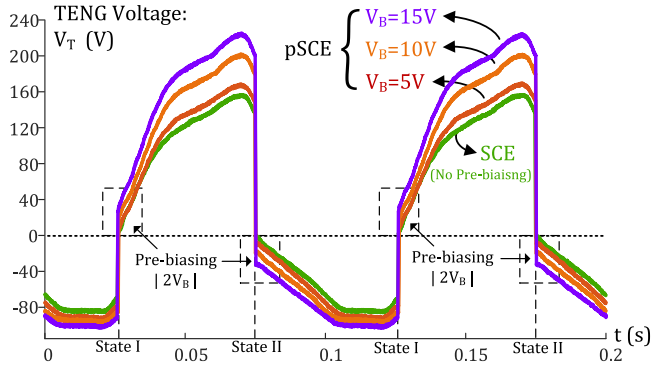

Fig. 14. Measured TENG Voltage V_T waveforms over two operation cycles for the SCE circuit and the pSCE circuit with load voltage V_B as 5 V, 10 V, and 15 V.

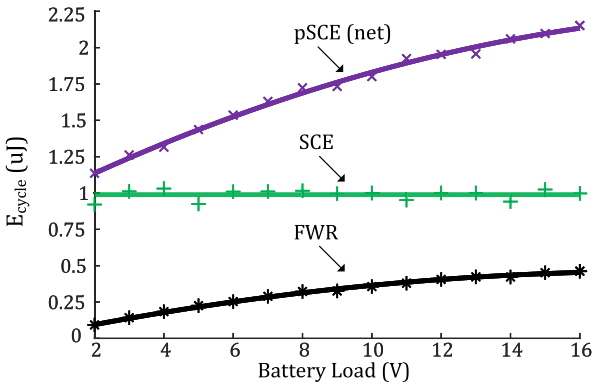

Fig. 15. Comparison of measured percycle energy for FWR, SCE, and pSCE circuit against the load voltage, V_B.

TABLE III
MEASURED ENERGY AND GAIN OF THE PSCE CIRCUIT OVER SCE AND FWR CIRCUIT AT DIFFERENT BATTERY LOAD

V_B (V)	E_{pSCE} (μJ)	$E_{\text{pre-bias}}$ (μJ)	$E_{\text{pSCE,net}}$ (μJ)	Gain over SCE	Gain over FWR
5	1.455	0.018	1.437	1.453	6.653
10	1.853	0.052	1.801	1.821	4.934
15	2.185	0.088	2.097	2.120	4.705

TABLE IV
EXPERIMENTAL POWER DENSITY OF THE FWR, SCE, AND THE PSCE CIRCUITS AT 10 V BATTERY LOAD

Circuit	PCB area (cm^2)	Power density (μW/cm^2)	PCB+TENG area (cm^2)	Power density (μW/cm^2)
FWR	1.290	2.829	113.790	0.032
SCE	11.413	0.867	146.413[a]	0.068
pSCE	15.435	1.167	150.435[a]	0.120

[a] includes Aux-TENG area

at 10 Hz operational frequency and 10 V battery load are listed in Table IV. It should be noted that we implement the TENG only for circuit validation using readily available material such as Aluminum and Teflon tape. The power density values can significantly improve for the real-world implementations using the recent advances in TENG materials and designs.

B. Comparison With EECs Reported in Literature

As mentioned in the Introduction, the CMEO defined in [11] sets the upper limit for energy extracted by any *passive* method (involving no pre-biasing) and serves as the reference for comparison, as has also been used in previous works such as [12] and [13]. Thus, for comparison, the percycle energy output (E_{cycle}) using different circuit architectures is first normalized against CMEO as

$$E_{\text{norm}} = \frac{E_{\text{cycle}}}{E_{\text{CMEO}}} \times 100\%;$$

$$E_{\text{CMEO}} = \frac{1}{2}\left(1 + \frac{1}{\beta}\right) C_{T,\min} V_{\text{oc,max}}^2.$$

Table V first lists the maximum theoretical output normalized to CMEO (E^*_{norm}) that the considered circuit architecture can achieve at its optimal load with *ideal circuit* implementation. As noted in *Remark 1*, SCE theoretically attains E_{CMEO} (implying its $E^*_{\text{norm}} = 100\%$) at all load voltages. In contrast, the proposed pSCE always outperforms SCE, and its energy output continues to grow with the load voltage leading to an unbounded E^*_{norm} (Refer *Remark 3*). Table V next lists the reported experimental load voltage and the measured E_{norm} at that voltage. The energy

TABLE V
PERFORMANCE COMPARISON WITH REPORTED EECS FOR TENG

Ref	Circuit architecture	Normalized maximum theoretical output (E^*_{norm}) and comment	Measurement load	Normalized experimental output (E_{norm})[a]
[24]	FWR	$\leq 25\%$ (max at $\beta = 1$)	26.75 V (Optimal)	20.43%
This work	FWR	$\leq 25\%$	15 V	11.37%
[28]	Half wave rectifier with parallel diode	50%	~58 V	15.49%
[12]	Synchronous switched serial/parallel capacitor	25% (depends on load and number of intermediate capacitors)	~90 V	23% (mechanical switching)
[13]	Synchronous parallel switch	$\leq 50\%$ (max at $\beta = 1$)	~70 V (Optimal)	~42.86% (mechanical switching)
[28]	Bennet voltage doubler	Unbounded; limited by air breakdown (needs $\beta > 2$)	~50 V	58.43%
[24]	P-SSHI	Limited by quality factor; high optimal load, so, impractical	15 V	19.53%
[24]	S-SSHI	Limited by quality factor; multiple transient cycles	26.15 V (Optimal)	172.8%
[14]	SCE	100% (capacitor load)	–	29.6%
[17]	SCE	100% (capacitor load)	–	37.8%
This Work	SCE	100% (battery load)	–	25.22%
This Work	pSCE	Unbounded; limited by air breakdown (161.72% at 15 V)	15 V	53.48%

[a] ignores control circuit energy consumption

outputs of FWR, S-SSHI, P-SSHI, and other such circuits listed in the table depend on load voltage, and an optimized load is needed to maximize the energy output, which requires an additional MPPT feature that consumes additional energy, and will reduce the net energy output. A key advantage of the proposed pSCE architecture is that it guarantees an energy output greater than CMEO at any load voltage as derived in (27).

IX. CONCLUSION

This work proposed *active* pre-biasing of TENG using the already present load battery for boosting the output energy beyond the SCE architecture, one that is proven to operate at CMEO, but in a *passive* setting. It was shown that the increase in output due to pre-biasing in the first half-cycle of TENG operation (separation of the TENG plates) is attributed to the increase in the transduced energy from the mechanical source. In contrast, the gain in the second half-cycle (retraction of plates) is due to a reduction in the dissipated TENG electrical (potential) energy into the environment. We showed that this loss could be reduced to zero by using an optimum pre-biasing voltage that sets the plate charges to zero. It was further shown that increasing the pre-biasing voltage increases the overall output, and the upper limit to pre-biasing is essentially determined by air dielectric-breakdown voltage or the level of available mechanical excitation, namely, till the electrostatic attraction due to pre-biasing becomes comparable to the external excitation force.

For implementation of the proposed technique, a pre-biased pSCE circuit was presented to enable the pre-biasing of TENG at the start of each half-cycle using the load battery. The energy output of the pSCE circuit and conditions on pre-biasing voltages for net-benefit over the SCE circuit were mathematically derived. Experimental implementation of the pSCE circuit validates the expected gain in the energy output. Using the pSCE circuit with 5 V battery load, experimental gains of 1.453 over the SCE circuit and 6.653 over the standard FWR circuit were achieved. A future research direction could explore the use of low-power active dc/dc converters to achieve optimum pre-biasing. We believe that the presented effort to increase the energy output by designing a novel pSCE circuit will bring us closer to the real-world feasibility of powering wireless sensor nodes by TENG.

ACKNOWLEDGMENT

The authors would like to thank Alex Denny of Rowe Electronics for PCB implementation of the circuits.

REFERENCES

[1] F. K. Shaikh and S. Zeadally, "Energy harvesting in wireless sensor networks: A comprehensive review," *Renewable Sustain. Energy Rev.*, vol. 55, pp. 1041–1054, 2016.
[2] Z. L. Wang, L. Lin, J. Chen, S. Niu, and Y. Zi, *Triboelectric Nanogenerators*. Berlin, Germany: Springer, 2016.
[3] J. Luo and Z. L. Wang, "Recent progress of triboelectric nanogenerators: From fundamental theory to practical applications," *EcoMat*, vol. 2, no. 4, 2020, Art. no. e12059.
[4] Z. L. Wang, T. Jiang, and L. Xu, "Toward the blue energy dream by triboelectric nanogenerator networks," *Nano Energy*, vol. 39, pp. 9–23, 2017.
[5] Z. Ren *et al.*, "Energy harvesting from breeze wind (0.7-6 m s- 1) using ultra-stretchable triboelectric nanogenerator," *Adv. Energy Mater.*, vol. 10, no. 36, 2020, Art. no. 2001770.
[6] Z. Ren, Z. Wang, F. Wang, S. Li, and Z. L. Wang, "Vibration behavior and excitation mechanism of ultra-stretchable triboelectric nanogenerator for wind energy harvesting," *Extreme Mechanics Lett.*, vol. 45, 2021, Art. no. 101285.
[7] J. Chen and Z. L. Wang, "Reviving vibration energy harvesting and self-powered sensing by a triboelectric nanogenerator," *Joule*, vol. 1, no. 3, pp. 480–521, 2017.
[8] S. S. Kwak, H. Kim, W. Seung, J. Kim, R. Hinchet, and S.-W. Kim, "Fully stretchable textile triboelectric nanogenerator with knitted fabric structures," *ACS Nano*, vol. 11, no. 11, pp. 10733–10741, 2017.
[9] L. Zhang *et al.*, "Enhancing the performance of textile triboelectric nanogenerators with oblique microrod arrays for wearable energy harvesting," *ACS Appl. Mater. Interfaces*, vol. 11, no. 30, pp. 26824–26829, 2019.
[10] S. Niu, Y. Liu, Y. S. Zhou, S. Wang, L. Lin, and Z. L. Wang, "Optimization of triboelectric nanogenerator charging systems for efficient energy harvesting and storage," *IEEE Trans. Electron Devices*, vol. 62, no. 2, pp. 641–647, Feb. 2015.
[11] Y. Zi, S. Niu, J. Wang, Z. Wen, W. Tang, and Z. L. Wang, "Standards and figure-of-merits for quantifying the performance of triboelectric nanogenerators," *Nat. Commun.*, vol. 6, no. 1, pp. 1–8, 2015.
[12] Y. Zi *et al.*, "An inductor-free auto-power-management design built-in triboelectric nanogenerators," *Nano Energy*, vol. 31, pp. 302–310, 2017.
[13] Y. Zi *et al.*, "Effective energy storage from a triboelectric nanogenerator," *Nat. Commun.*, vol. 7, 2016, Art. no. 10987.
[14] X. Cheng *et al.*, "High efficiency power management and charge boosting strategy for a triboelectric nanogenerator," *Nano Energy*, vol. 38, pp. 438–446, 2017.
[15] F. Xi *et al.*, "Universal power management strategy for triboelectric nanogenerator," *Nano Energy*, vol. 37, pp. 168–176, 2017.

[16] K. Rawy *et al.*, "A triboelectric nanogenerator energy harvesting system based on load-aware control for input power from 2.4 μw to 15.6 μw," *Nano Energy*, vol. 74, 2020, Art. no. 104839.
[17] H. Wu, H. Li, and X. Wang, "A high-stability triboelectric nanogenerator with mechanical transmission module and efficient power management system," *J. Micromechanics Microengineering*, vol. 30, no. 11, 2020, Art. no. 115017.
[18] X. Cheng, W. Tang, Y. Song, H. Chen, H. Zhang, and Z. L. Wang, "Power management and effective energy storage of pulsed output from triboelectric nanogenerator," *Nano Energy*, vol. 61, pp. 517–532, 2019.
[19] M. Perez, S. Boisseau, M. Geisler, G. Despesse, and J. L. Reboud, "A triboelectric wind turbine for small-scale energy harvesting," in *Proc. J. Phys.: Conf. Ser.*, IOP Publishing, 2016, vol. 773, no. 1, Art. no. 012118.
[20] E. Lefeuvre, A. Badel, C. Richard, and D. Guyomar, "Piezoelectric energy harvesting device optimization by synchronous electric charge extraction," *J. Intell. Mater. Syst. Struct.*, vol. 16, no. 10, pp. 865–876, 2005.
[21] J. Dicken, P. D. Mitcheson, I. Stoianov, and E. M. Yeatman, "Power-extraction circuits for piezoelectric energy harvesters in miniature and low-power applications," *IEEE Trans. Power Electron.*, vol. 27, no. 11, pp. 4514–4529, Nov. 2012.
[22] K. A. Singh, M. Pathak, R. J. Weber, and R. Kumar, "A self-propelled mechanism to increase range of bistable operation of a piezoelectric cantilever-based vibration energy harvester," *IEEE Trans. Ultrason., Ferroelect., Freq. Control*, vol. 65, no. 11, pp. 2184–2194, Nov. 2018.
[23] M. Pathak and R. Kumar, "Modeling and analysis of energy extraction circuits for triboelectric nanogenerator based vibrational energy harvesting," *SPIE*, vol. 10663, 2018, Art. no. 106630F.
[24] M. Pathak and R. Kumar, "Synchronous inductor switched energy extraction circuits for triboelectric nanogenerator," *IEEE Access*, vol. 9, pp. 76938–76954, 2021.
[25] S. Xu, W. Ding, H. Guo, X. Wang, and Z. L. Wang, "Boost the performance of triboelectric nanogenerators through circuit oscillation," *Adv. Energy Mater.*, vol. 9, no. 30, 2019, Art. no. 1900772.
[26] X. Li and Y. Sun, "An SSHI rectifier for triboelectric energy harvesting," *IEEE Trans. Power Electron.*, vol. 35, no. 4, pp. 3663–3678, Apr. 2020.
[27] I. Kara, M. Becermis, M. A.-A. Kamar, M. Aktan, H. Dogan, and S. Mutlu, "A 70-to-2 V triboelectric energy harvesting system utilizing parallel-SSHI rectifier and DC-DC converters," *IEEE Trans. Circuits Syst. I: Reg. Papers*, vol. 68, no. 1, pp. 210–223, Jan. 2021.
[28] A. Ghaffarinejad *et al.*, "A conditioning circuit with exponential enhancement of output energy for triboelectric nanogenerator," *Nano Energy*, vol. 51, pp. 173–184, 2018.
[29] W. Liu *et al.*, "Integrated charge excitation triboelectric nanogenerator," *Nat. Commun.*, vol. 10, no. 1, pp. 1–9, 2019.
[30] X. Xia, H. Wang, P. Basset, Y. Zhu, and Y. Zi, "Inductor-free output multiplier for power promotion and management of triboelectric nanogenerators toward self-powered systems," *ACS Appl. Mater. Interfaces*, vol. 12, no. 5, pp. 5892–5900, 2020.
[31] A. D. Elliott and P. D. Mitcheson, "Implementation of a single supply pre-biasing circuit for piezoelectric energy harvesters," *Procedia Eng.*, vol. 47, pp. 1311–1314, 2012. [Online]. Available: https://www.sciencedirect.com/science/article/pii/S1877705812044591
[32] S. Niu *et al.*, "Simulation method for optimizing the performance of an integrated triboelectric nanogenerator energy harvesting system," *Nano Energy*, vol. 8, pp. 150–156, 2014.
[33] P. D. Mitcheson and T. C. Green, "Maximum effectiveness of electrostatic energy harvesters when coupled to interface circuits," *IEEE Trans. Circuits Syst. I: Reg. Papers*, vol. 59, no. 12, pp. 3098–3111, Dec. 2012.
[34] A. Karami, A. Dudka, D. Galayko, F. Marty, and P. Basset, "The limiting effect of electromechanical coupling in self-biased electrostatic vibration energy harvester," in *Proc. IEEE Symp. Design, Test, Integration Packag. MEMS/MOEMS*, 2015, pp. 1–4.
[35] H. Li, C. Tian, and Z. D. Deng, "Energy harvesting from low frequency applications using piezoelectric materials," *Appl. Phys. Rev.*, vol. 1, no. 4, 2014, Art. no. 041301.

Madhav Pathak (Graduate Student Member, IEEE) received the B.Tech. degree in electrical engineering from IIT Roorkee, Roorkee, India, in 2016. He is currently working toward the Ph.D. degree in electrical engineering with Iowa State University, Ames, IA, USA.

His research interests include the design of ambient micro energy harvesters and power management circuits for Internet of Things (IoT) applications.

Pathak was a recipient of the Indian Academy of Science Summer Research Fellowship in 2014, the Honda Young Engineer and Scientist Award in 2014, the DAAD WISE Scholarship by the German Academic Exchange Service in 2015, and the NSF-INTERN Award in 2018 and 2019.

Ratnesh Kumar (Fellow, IEEE) received the B.Tech. degree in electrical engineering from IIT Kanpur, Kanpur, India, in 1987, and the M.S. and Ph.D. degrees in electrical and computer engineering from The University of Texas at Austin, TX, USA, in 1989 and 1991, respectively.

He is currently a Palmer Professor with the Electrical and Computer Engineering Department, Iowa State University, Ames, IA, USA, where he directs the ESSeNCE (Embedded Software, Sensors, Networks, Cyberphysical, and Energy) Lab. Previously, he held Faculty Position with the University of Kentucky, Lexington, KY, USA, and various visiting positions with the University of Maryland, College Park, MD, USA, the Applied Research Laboratory with the Pennsylvania State University, State College, PA, USA, the NASA Ames, the Idaho National Laboratory, the United Technologies Research Center, and the Air Force Research Laboratory.

Dr. Kumar was a recipient of the gold medals for the Best EE Undergrad, the Best EE Project, and the Best All Rounder from IIT Kanpur, the Best Dissertation Award from UT Austin, the Best Paper Award from the IEEE TRANSACTIONS ON AUTOMATION SCIENCE AND ENGINEERING, and Keynote Speaker and paper awards recipient from multiple conferences. He is or has been an editor of several journals (including of IEEE, SIAM, ACM, Springer, IET, MDPI), was a Distinguished Lecturer of the IEEE Control Systems Society, is a recipient of D. R. Boylan Eminent Faculty Award for Research from Iowa State University and also a Fellow of AAAS (American Association for the Advancement of Science).